Effect of multiple substorms on the buildup of the ring current

Kristi A. Keller
SP Systems Inc., NASA Goddard Space Flight Center, Greenbelt, Maryland, USA

Mei-Ching Fok, Ayris Narock, Michael Hesse, Lutz Rastaetter, and Maria M. Kuznetsova
NASA Goddard Space Flight Center, Greenbelt, Maryland, USA

Tamas I. Gombosi and Darren L. DeZeeuw
Space Physics Research Laboratory, University of Michigan, Ann Arbor, Michigan, USA

Received 16 August 2004; revised 12 January 2005; accepted 4 February 2005; published 13 August 2005.

[1] The effect of magnetospheric substorms on the ring current is not completely understood. Using a combination of the University of Michigan's BAT-S-RUS Model and Fok Ring Current Model, we modeled the effects of multiple substorms on the ring current by modeling multiple dipolarizations in the tail. Increasing the number of substorms corresponds to increases in the number of injections into the ring current. The ionospheric potential increases during periods of southward IMF. Energy increases are more dependent on the duration of large ionospheric potential than the number of substorm dipolarizations.

Citation: Keller, K. A., M.-C. Fok, A. Narock, M. Hesse, L. Rastaetter, M. M. Kuznetsova, T. I. Gombosi, and D. L. DeZeeuw (2005), Effect of multiple substorms on the buildup of the ring current, *J. Geophys. Res.*, *110*, A08202, doi:10.1029/2004JA010747.

1. Introduction

[2] An outstanding issue in ring current dynamics is the role that substorms play in ring current buildup during a magnetic storm. *Akasofu* [1968] described the cause of the typical magnetospheric storm as a compression of the magnetosphere followed by a series of magnetospheric substorms. In this view, substorms would contribute significantly to the ring current buildup during the main phase of the magnetic storms. In another view, *Kamide* [1992] thought that enhanced convection during southward interplanetary magnetic field (IMF) for a prolonged period of time drove the magnetic storm. Kamide noted that substorms always occurred during magnetic storms because the southward IMF would also drive substorms. He proposed that it was possible that substorms did not drive magnetic storms but that substorm and storms were independent processes both driven by southward IMF.

[3] In terms of the ring current, this issue becomes a question of the relative importance of the processes that energize the particles. One view holds the idea that a period of prolonged southward IMF forms the ring current by driving increased convection in the magnetosphere, causing particle injections into the inner magnetosphere [e.g., *Wolf and Harel*, 1979]. Simulation studies by *Harel et al.* [1981] and *Wolf et al.* [1997] have shown that a ring current could be generated by enhanced global convection. In this case, the important factors for the formation of the ring current would be the large-scale electric field that would serve as the driver and the plasma sheet density that would serve as the source population for the newly formed ring current. *Ebihara and Ejiri* [2000] found that the convective electric field and plasma density could account for the major variations of *Dst**. This large-scale electric field is driven by the southward IMF. In this case, substorms would not contribute significantly to the buildup of the ring current. Some simulation studies have found that enhancements in the phase space density in the plasma sheet are also required to account for observed changes in *Dst* [*Chen et al.*, 1994; *Jordanova et al.*, 1998; *Kozyra et al.*, 1998].

[4] In the other view, substorms are thought to contribute significantly to the energization of the ring current through dipolarization of the magnetic field. The dipolarization would cause an inductive electric field that would contribute to particle acceleration. *Fok and Moore* [1997] found that electric fields induced by dipolarization could play a major role in injecting particles into the ring current in their model. In another study, *Fok et al.* [1996] found that the effect of dipolarization depends on the large-scale electric field. During the early main phase when the convection field is small, they found that the ring current was smaller if inductive electric fields were included than with the case of a steady magnetic field. When the convection had increased during the later main phase, they found that the increase in ring current energy was similar for both cases. They suggested that the effect of dipolarization depended on the drift paths. In particular, under stronger large-scale electric fields the injected particles from dipolarization would move closer to the Earth and would be less likely to be lost on the dayside. *Fok et al.* [1999] used a particle tracing code to inject particles on the nightside boundary to create a more realistic outer boundary. Using this boundary condition, they simulated substorms within a storm and

0148-0227/05/2004JA010747

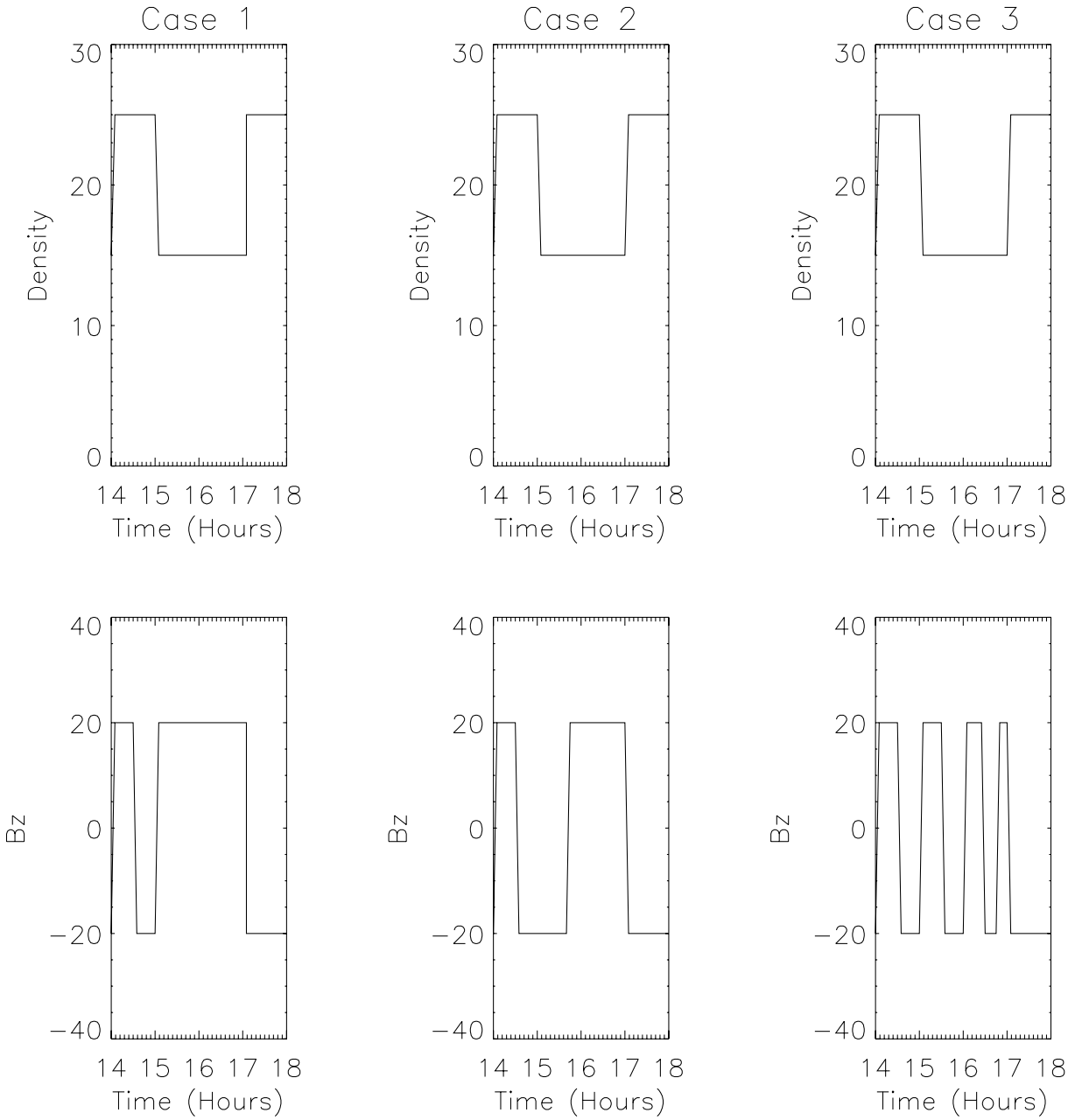

Figure 1. The solar wind input for the two cases. The left column shows case 1, the middle column shows case 2, and the right column shows case 3. The top row is the density. The bottom row is B_z. The velocity in both cases was a constant 450 km/s.

substorms without a storm. They found that substorms during a storm produced larger proton energy within geosynchronous orbit than the case of a substorm without a storm. They also simulated storms with and without substorms. The proton energy within 12 R_E during the storm was similar in both the substorm and no substorm case. In the substorm case without a storm, the proton energy increased within 12 R_E but most of the increase in energy stayed outside of geosynchronous orbit. They also simulated a case of a storm without a substorm. In that case, most of the increase in total proton energy stayed outside of geosynchronous orbit. These results suggest that both substorms and a strong convective electric field are needed to increase proton energy inside geosynchronous orbit. Observational studies [*Reeves et al.*, 2004; *Reeves and Henderson*, 2001; *Lui et al.*, 2001] concluded that both substorms and strong convective electric field are required for buildup of the storm-time ring current.

[5] Do multiple substorms increase the total proton kinetic energy of the ring current as compared with isolated substorms? This research will use the Fok Ring Current Model driven by the University of Michigan BATS-R-US global magnetospheric MHD simulation to explore the role substorms play in the buildup of the ring current. In particular we will describe how the symmetry and energy of the ring current are different for multiple substorms as

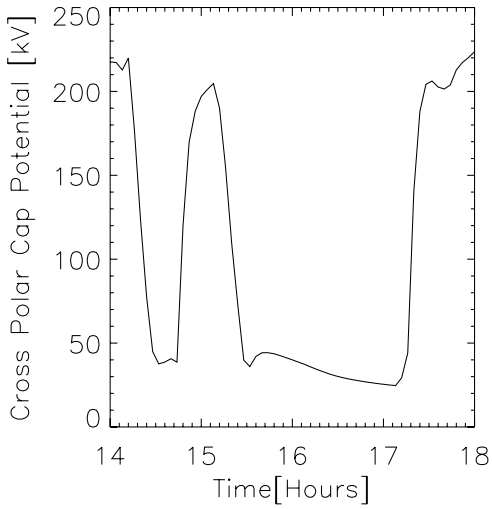

Figure 2. The cross polar cap potential for the Northern Hemisphere for case 1.

compared with isolated substorms. We will also describe how multiple substorms can drive injections into the ring current.

2. Description of the Computer Models

[6] The combined model starts with solar wind input. The BATS-R-US MHD magnetosphere model uses this input as an upstream boundary condition. The BATS-R-US MHD model [*Powell et al.*, 1999] calculates, self-consistently, a magnetic field, ionospheric potential, and plasma sheet temperature and density distributions that are then used as input to the Fok Ring Current Model. Using these inputs, the Fok Ring Current Model [*Fok et al.*, 1995, 1999; *Fok and Moore*, 1997] calculates the differential particle fluxes for protons and electrons up to 300 keV by solving a bounce-averaged Boltzmann transport equation for a phase space distribution function along magnetic field lines. The phase space distribution is assumed to be constant along magnetic field lines. The convection terms include gradient-curvature drift and $\mathbf{E} \times \mathbf{B}$ drift. The $\mathbf{E} \times \mathbf{B}$ drift term includes both corotation and the ionospheric potential. In addition, the model calculates losses due to charge exchange. The initial source population uses the quiet time ion composition compiled by *Sheldon and Hamilton* [1993], which were obtained using Active Magnetospheric Particle Tracer Explorer/Charge Composition Explorer/Charge-Energy-Mass instrument. After the initial time step of the ring current, the ring current uses the MHD temperature and density at the outer boundary (10 R_E on the nightside and the last closed field line on the dayside) of the ring current model. The pitch-angle distribution on the boundary is also assumed to be isotropic.

3. Solar Wind Boundary Condition

[7] This paper compares three cases of simplified solar wind parameters for the evolution of the ring current. These cases have an identical startup phase that includes running the ring current driven by the MHD model for 4 hours. This startup period had 2 hours of 20 nT B_z followed by 2 hours of -20 nT B_z. After this startup, the IMF is turned northward and the solar wind density is increased to 25 cm^{-3}. In case 1, the IMF is turned southward at the boundary twice at 1430 and 1705 and has a period of northward IMF from 1505 to 1705. The density is decreased at 1505 to 15 cm^{-3}. At 1705, the solar wind density is increased to 25 cm^{-3}. The solar wind density profile was chosen to be similar to density profiles in two storms that we studied using ACE solar wind data. Future work will study how different density profiles impact the buildup of the ring current. In case 2, the IMF is turned southward at the boundary twice at 1430 and 1705 and has a period of northward IMF from 1545 to 1705. The period of southward IMF is 40 min longer than the case 1. The solar wind density profile is the same as in case 1. In case 3, the IMF is turned southward on four different occasions. The solar wind density profile is the same as in case 1. The duration of southward IMF is the same as case 2. As we will discuss in greater detail in the next section, a substorm occurs roughly 25–45 min each time after the southward IMF impacts the magnetosphere. For case 1 and 2 this means that there are two substorms spaced approximately 2.5 hours apart. For case 3 there are four substorms in the same time period. Figure 1 shows the solar wind data for the three cases. The velocity is kept constant at 450 km/s. The comparison between the first two cases looks at the importance of the duration of large ionospheric potentials in energizing the ring current. The comparison between cases 2 and 3 looks at the importance of the number of substorms in energizing the ring current.

4. Magnetosphere Simulation

4.1. Case 1

[8] Figure 2 shows the cross polar cap potential for the northern hemisphere for case 1. There are two increases in the cross polar cap potential following the IMF turning southward. The first interval of southward IMF occurred from 1440 to 1508. The sequence of events in the simulation is fairly typical of all the intervals of southward IMF. Figure 3 shows a sequence of plots of the magnetic field lines for this interval. Figure 4 shows a sequence of ring current plots in the SM equatorial plane for the same time interval. Figures 3a and 4a show the magnetosphere and ring current before the impact of the southward IMF on the magnetopause. At 1440, the southward IMF impacts the magnetosphere. After 1448, the potential increases in ionosphere (Figure 2), the tail stretches (Figures 3b–3d), the magnetopause moves inward as shown by the ring current boundary moving inward (Figures 4b–4d), and there is a decrease of flux on the prenoon sector of the magnetosphere (Figures 4b–4f). At 1504, reconnection occurs in the near tail region and a plasmoid is seen in the tail (Figures 3e–3f). Starting at 1508, an injection is seen around geosynchronous orbit (Figures 4e–4f).

[9] At 1508 the IMF turns northward at the magnetosphere. The magnetosphere expands outward. Around 1600 the ring current becomes symmetric. Figures 5a–5b show the symmetry at 1632 and 1712. The second interval of southward IMF starts at 1708. Starting around 1720, the potential increases again (Figure 2), the tail stretches, and the magnetopause moves inward. This is similar to the

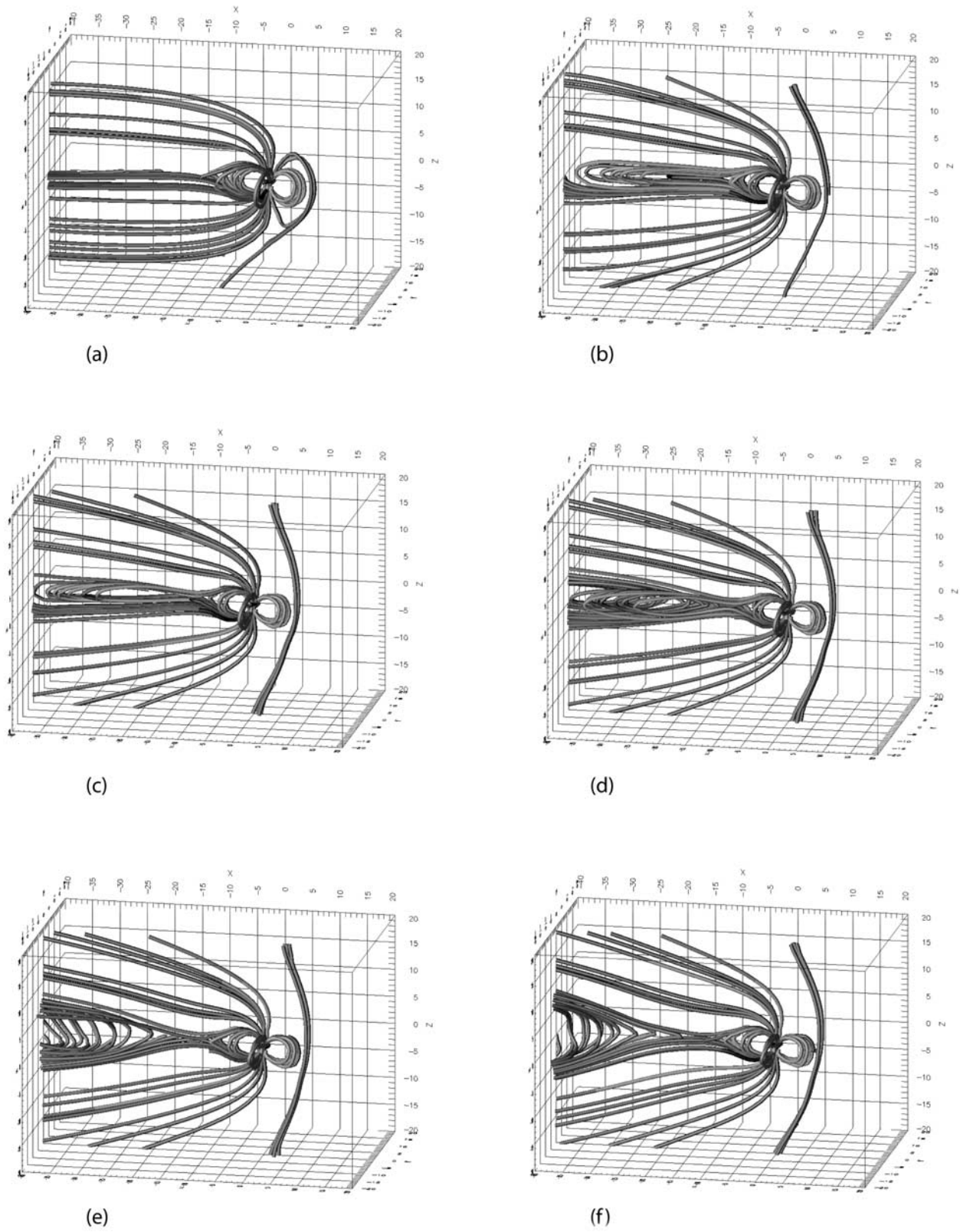

Figure 3. Plots of the magnetic field lines for case 1 at times (a) 1436, (b) 1452, (c) 1456, (d) 1500, (e) 1504, and (f) 1508.

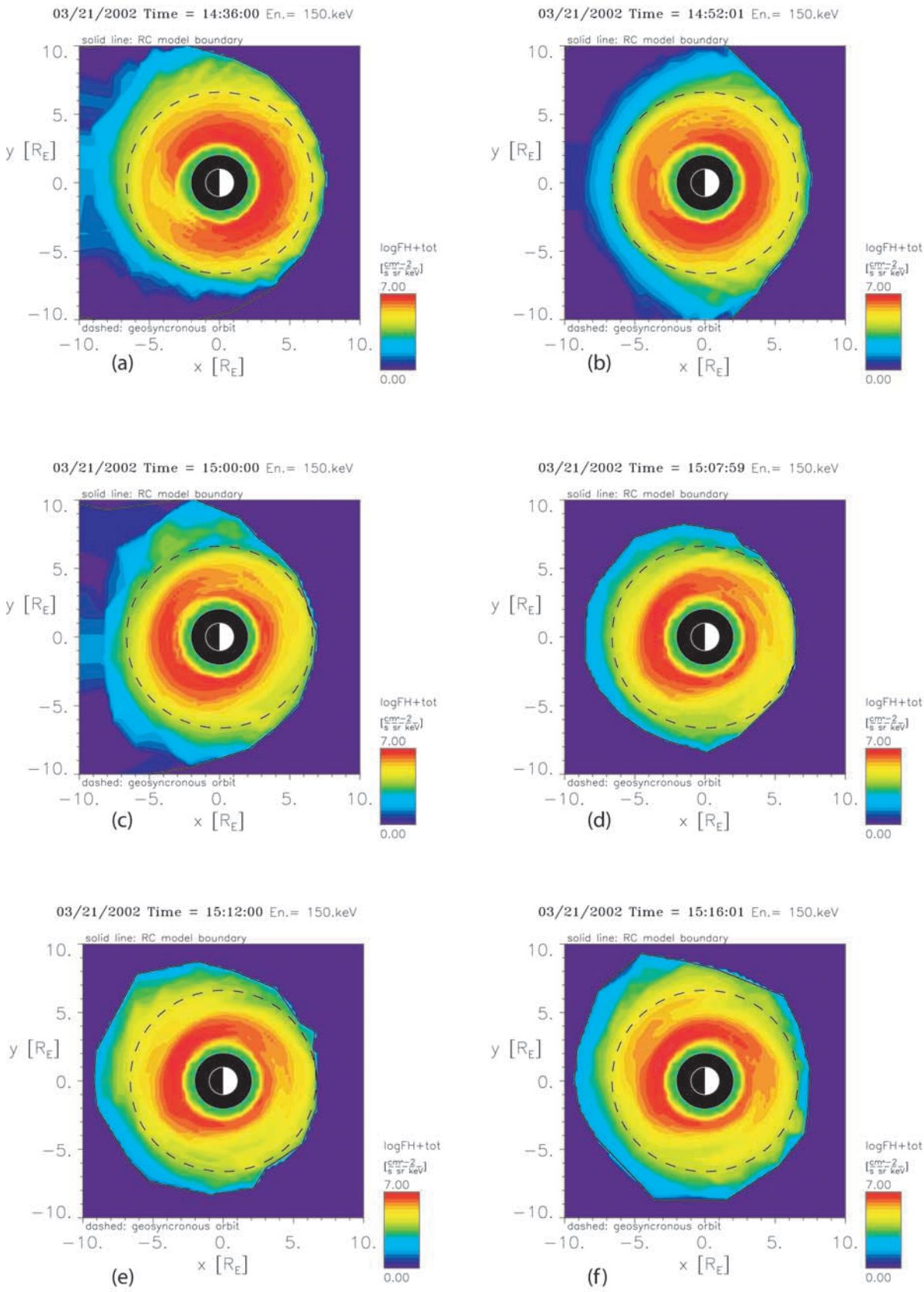

Figure 4. Plots of ring current for case 1 at times (a) 1436, (b) 1452, (c) 1500, (d) 1508, (e) 1512, and (f) 1516.

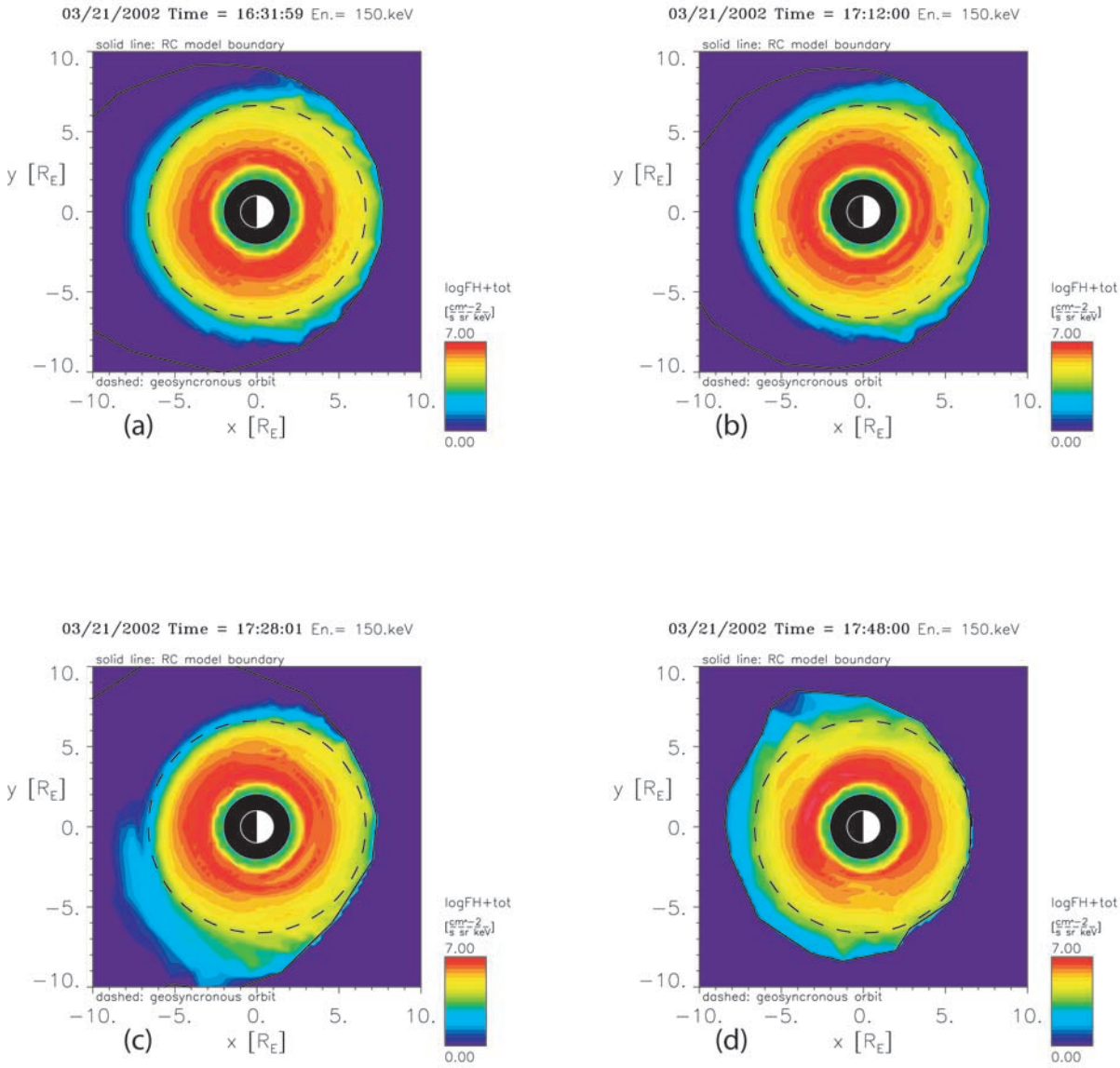

Figure 5. Plots of ring current for case 1 at times (a) 1632, (b) 1712, (c) 1728, and (d) 1748.

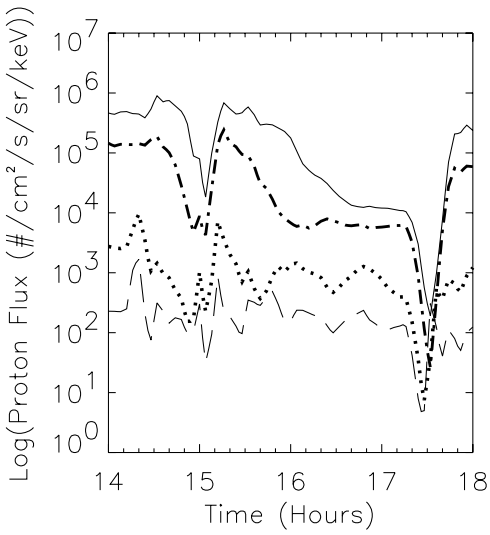

Figure 6. Plot of the proton flux at geosynchronous orbit at 2100 MLT for case 1. The different lines represent energies of 62.5 keV (solid), 141.5 keV (dotted-dashed), 210 keV (dotted), and 300 keV (dashed).

sequence of events during the first interval of southward IMF except that the decrease of proton flux on the prenoon side is smaller. At 1728 a flux dropout can be seen at geosynchronous orbit on the nightside (Figure 5c). In this case reconnection occurs at 1744. This is later than in the first interval of southward IMF. A plasmoid is seen in the tail at 1748. When reconnection occurs, an injection can be seen near geosynchronous orbit (Figure 5d).

[10] Figure 6 shows the proton flux at geosynchronous orbit at 2100 MLT. There is a small increase in the flux, especially at 210 keV after the potential increases at 1448. At the time of reconnection (1504), there is a sharp increase in the proton flux at all the energies. After the increase, drift echoes are seen in the flux for two highest energies, which then becomes level until the next interval of southward IMF. The flux for 62.5 keV decreases significantly. This is due to weaker convection during this time period. A decrease is seen in the flux starting near 1720, with the minimum being reached around 1728. The flux increases in all the energies after 1730.

4.2. Case 2

[11] The IMF is turned southward at the same time in case 1 but remains southward longer (Figure 1). This increases the time of large ionospheric potentials (Figure 7) and strong convection in the ionosphere. The first injection is the same as the first case. As in case 1, the ring current becomes symmetric during the period of northward IMF except that the proton flux is higher at 4 and 5 R_E (Figure 8a). After the second southward turning of the IMF, there is a flux dropout similar to the first case (Figure 8b). The second injection is seen near geosynchronous orbit around 1740 (Figures 8c–8d).

[12] Figure 9 shows the proton flux at geosynchronous orbit at 2100 MLT. As in case 1, there is a small increase in the flux, especially at the highest energy, after the potential increases at 1448, followed by a sharp increase in the proton flux at all the energies after reconnection. After the injection, the flux remains fairly constant or slight decreases until the IMF turns northward. At this point there is a decrease in flux, especially in the lower two energies, 62.5 keV and 141.5 keV. The flux dropout occurs around 1718. The flux increases in all the energies after 1730.

4.3. Case 3

[13] The first interval of southward IMF is identical to the first case, and ring current flux is shown in Figure 4. The second interval of southward IMF runs from 1538 to 1608. While the sequence of events in the second interval is very similar to the first interval, there are some differences. The solar wind density during the second interval is 15 cm^{-3}, which is smaller than the solar wind density during the first interval of southward IMF. Also, the potential increase is smaller (Figure 10). For the ring current, only a small decrease in proton flux on the dayside is seen and the particle injection is smaller. Figure 11a shows that case 3 has a smaller flux in the prenoon sector during the interval of northward IMF as compared with case 2 (Figure 8a). The third interval is from 1634 to 1652. This has the smallest interval of southward IMF. In this case, the potential increase is smaller than the two previous cases (Figure 10). The magnetopause moves in slightly and dayside losses are small. A plasmoid is still released, but only a slight injection is seen inside geosynchronous orbit (Figure 11b). The fourth interval of southward IMF occurs from 1708 to 1800. One difference in this interval from the preceding case is that the dipolarization is significantly smaller and the plasmoid is very small compared with previous intervals. The potential increase is comparable to the first interval. Figures 11c–11d show the ring current for this interval. The injection for this interval (Figure 11d) is at geosynchronous orbit and is in a similar location as compared with the first injection (Figure 4f) but smaller.

[14] Figure 12 shows the proton flux at geosynchronous orbit at 2100 MLT. It is similar to the first case until 1540. At 1556 there is an increase in flux for energies 62.5, 141.5, and 210 keV due to the potential increase. After reconnection there is another increase in flux for those energies. A third increase occurs with the third interval of southward

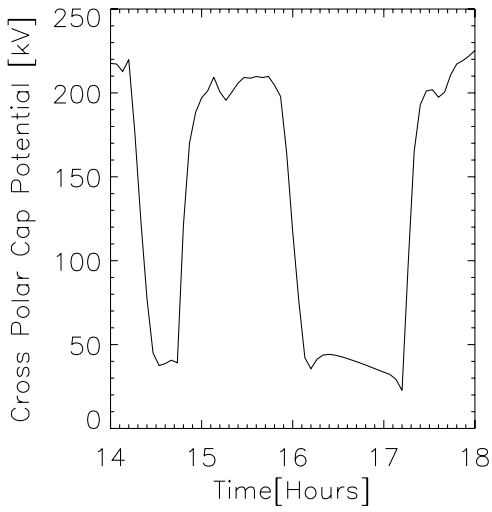

Figure 7. The cross polar cap potential for the Northern Hemisphere for case 2.

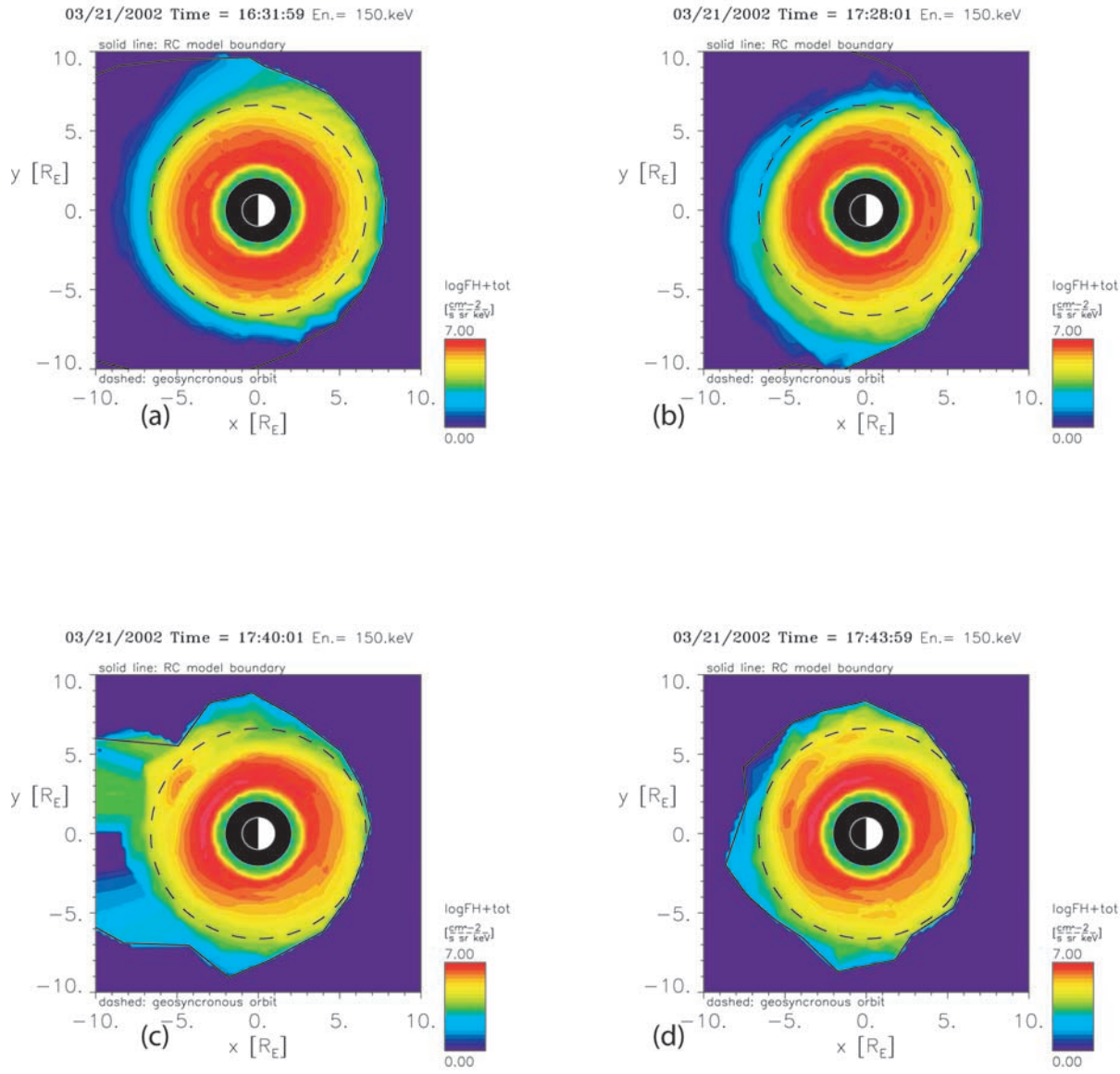

Figure 8. Plots of ring current for case 2 at times (a) 1632, (b) 1728, (c) 1740, and (d) 1744.

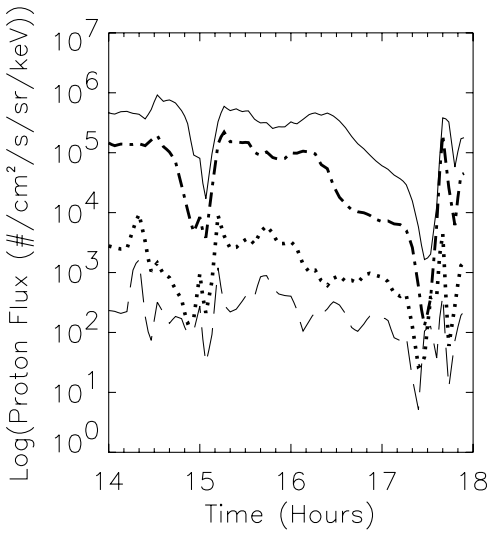

Figure 9. Plot of the proton flux at geosynchronous orbit at 2100 MLT for case 2. The different lines represent energies of 62.5 keV (solid), 141.5 keV (dotted-dashed), 210 keV (dotted), and 300 keV (dashed).

IMF but this corresponds to the potential increase. The third increase in flux is smaller than the increases for the previous two intervals. The last increase can be seen in all four energies but is smaller for the lower two energies.

4.4. Comparison

[15] There are two main differences between case 1 and case 2. The fluxes in case 2 tend to be higher during the interval between the two injections. The flux at energies 62.5 and 141.5 keV stays higher in case 2 than in case 1 after 1550 until the flux dropout. The flux for 210 keV stays higher for 30 min in case 2 than for case 1. The second major difference is the second injection in case 2 is larger than the second injection in case 1. The first difference is related to the longer duration of strong convection in case 2 that allows a longer period of energization. The differences in the particle populations prior to the second injection contribute to the larger injection in case 2.

[16] There are two main differences between case 2 and case 3. Case 3 has more injections than case 2. This difference is related to the number of substorms in the tail. The second major difference is that a flux dropout around geosynchronous orbit occurs for case 2 during the last interval of southward IMF as shown in Figure 8c. As the tail stretches (substorm growth phase), conservation of the third adiabatic invariant causes drift shells to expand to higher L and at the same time particles lose energy causing a flux dropout [*Baker and McPherron*, 1990; *Delcourt and Sauvaud*, 1994; *Sauvaud et al.*, 1996; *Fok et al.*, 1999]. Future studies will consider under what conditions flux dropouts occur in the combined model.

5. Energy in the Ring Current

[17] In this section we will discuss how the energy of the protons in the ring current is affected by multiple substorms. For cases 1 and 2, the southward IMF hits the magnetopause around 1440 and 1708. For case 3, the southward IMF hits the magnetopause around 1440, 1538, 1634, and 1708. Figure 13a shows the total proton kinetic energy within geosynchronous orbit for case 1 (solid line), case 2 (dotted line), and case 3 (dashed line). For case 1, injections in the ring current occur around 1504 and 1744 and correspond to the second and third increases in the energy for the ring current. For case 2, injections occurred around 1504 and 1744 and correspond to the second and fourth increases in the ring current. For case 3, injections occurred around 1504, 1612, and 1708. These correspond to the last three increases in energy in the ring current. There is a fourth injection around 1732. At this time, the total proton energy stays fairly constant. In case 3, the increases in energy are smaller for the later injections. During this time period, the peaks in density at the nightside boundary are smaller. For the third injection, the ionospheric potential and the temperature at the nightside boundary are also smaller. For all cases, there are large decreases in energy after a southward turning prior to the injection. The decreases in energy occur when there are decreases in the number of particles within geosynchronous orbit (Figure 13b) and when the tail magnetic field is being stretched. There are increases in the number of particles that correspond to injections in the ring current. Figure 13c shows the mean energy within geosynchronous orbit for all cases. For all cases, the mean energy increases after injections. During periods of southward IMF, the mean energy increases more than during periods of northward IMF. The mean energy increase is due to energy increases from larger convection and also due to increased losses of lower energy particles out the dayside. Both cases 1 and 2 show decreases in mean energy during the flux dropout. The highest mean energy at the end of the simulation is for case 3, while case 1 has the lowest mean energy.

[18] One mechanism for increasing and decreasing energy into the ring current is losses and gains of particles through the boundary. Figure 13d shows the energy lost through the dayside by particles being lost through the boundary.

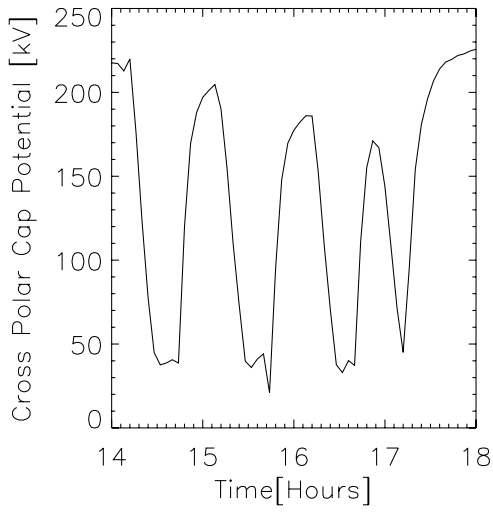

Figure 10. The cross polar cap potential for the Northern Hemisphere for case 3.

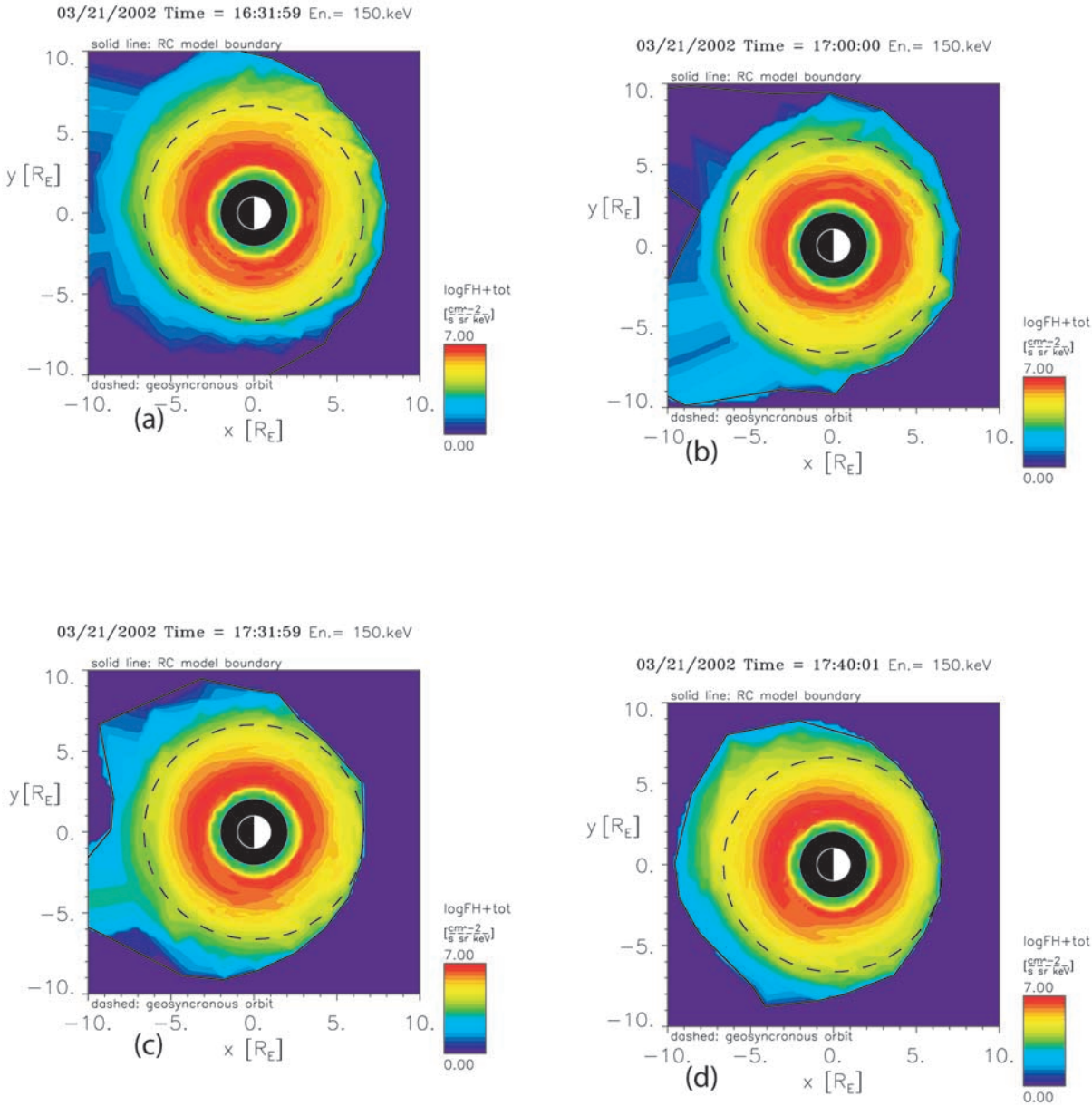

Figure 11. Plots of ring current for case 3 at times (a) 1632, (b) 1700, (c) 1732, and (d) 1740.

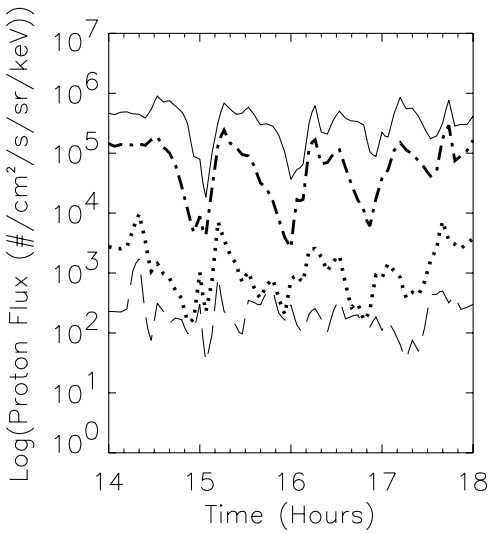

Figure 12. Plot of the proton flux at geosynchronous orbit at 2100 MLT for case 2. The different lines represent energies of 62.5 keV (solid), 141.5 keV (dotted-dashed), 210 keV (dotted), and 300 keV (dashed).

Figure 13e shows the energy gained through the nightside boundary. Figures 13d and 13e are plots of cumulative energy changes for the boundaries. The slope of the curve indicates where losses and gains occur. Whenever the curve is flat, there are no additional losses or gains in energy. There are large losses on the dayside approximately 12 min after the IMF turns southward. Approximately 6–8 min after the southward turning, the potential starts to increase and the magnetopause moves inward on the dayside. Reconnection on the dayside changes closed field lines to open field lines and the open/closed field boundary moves closer to the Earth. Case 3 has a larger loss after 1740. The potential for case 3 is slightly higher than for either case 1 or case 2 from 1720 onward. Since the southward IMF continues to the end of the simulation, the magnetopause remains compressed and the potential stays high. This contributes to continual losses out the dayside. There are large increases in energy on the nightside approximately 12 min after each time the IMF turns southward. In the MHD code at this time, there are increases in the density at 10 R_E. The increases in energy on the nightside boundary correspond to the losses on the dayside. These changes are not enough to account for the changes in total energy.

[19] Besides losses and gains through the boundary, there are other processes that can contribute to energy losses and gains within the simulation domain. Figure 13f shows the losses due to charge exchange. In this case the losses are very similar for all cases. Also, these losses are significantly smaller than the losses on the dayside boundary. This result is consistent with *Liemohn et al.* [1999]. Figure 13g shows energy gains due to adiabatic acceleration due to drift. This acceleration is due to an increase in convection. As convection is increased, particles are pushed toward the Earth into regions of larger magnetic field. The increases due to drift occur near the same time as reconnection. This is approximately 15–20 min after the potential increase. During the third interval of southward IMF for case 3, there is no increase in energy due to the drift terms. The potential increase and the density and temperature at the nightside boundary were smaller during this interval. The increases in energy due to adiabatic acceleration due to drift occur slightly before the injections and the increases in mean energy shown in Figure 13c. Figure 13h shows the energy changes due to changes in the magnetic field at the particle location. The decreases occur during intervals of southward IMF before reconnection. During this time period, the magnetic field in the tail stretches and energy is lost due to adiabatic effects. There is also a loss of particles within geosynchronous orbit. There are also changes in energy due to magnetic field changes on the dayside. After reconnection and during periods of northward IMF, an increase in the number of particles and changes in the magnetic field cause an increase in the total energy. The mean energy increases after reconnection during periods of southward IMF and for approximately 15 min after the IMF turns northward and then stays constant until the next reconnection event. After reconnection, the energy increases are fairly small, since the main changes in the magnetic field occur outside 10 R_E and are not within the boundary of the ring current model. When the IMF is northward, there is an increase in the magnitude of the magnetic field on the dayside. During the last interval of southward IMF for case 3, there is no increase in energy due to the change in the magnetic field and the number of particles within geosynchronous orbit continues to decrease. There is an increase in energy due to the adiabatic acceleration due to drift. The increase in total energy is smaller than the first increase at 1508 for cases 1 and 3. For case 2, the last interval of southward turning produces a large increase in total energy. The changes in energy seen in Figure 13a are due to a combination of energy gains due to the changing magnetic field and gains due to adiabatic acceleration due to drift terms. The overall energy gain occurs due to the drift terms and the oscillations in the total energy are due to the changes in magnetic field. Energy losses seen in Figure 13a are mainly due to the magnetic field in the tail stretching, changes in the magnetic field on the dayside, and a loss of particles within geosynchronous orbit.

6. Summary

[20] Do multiple substorms increase the total proton kinetic energy of the ring current as compared with isolated substorms? Under these conditions, multiple substorms do not increase the total proton kinetic energy. Only case 2 with two isolated substorms had a significant increase in total energy (about 35%). The duration of southward IMF has bigger impact on the mean proton energy than the number of substorms. Cases 2 and 3 had the same duration of southward IMF. Case 3 had the largest increase in mean energy (1.75 times the original energy). Case 2 had a smaller increase in mean energy (1.56 times the original energy). Both were larger than Case 1 (1.21 times the original energy). Case 3 had four substorms, as compared with two substorms for cases 1 and 2. Case 3 had a lower number of particles within geosynchronous orbit. In case 3, the dayside boundary was near geosynchronous orbit a significant amount of time, causing a larger loss of particles

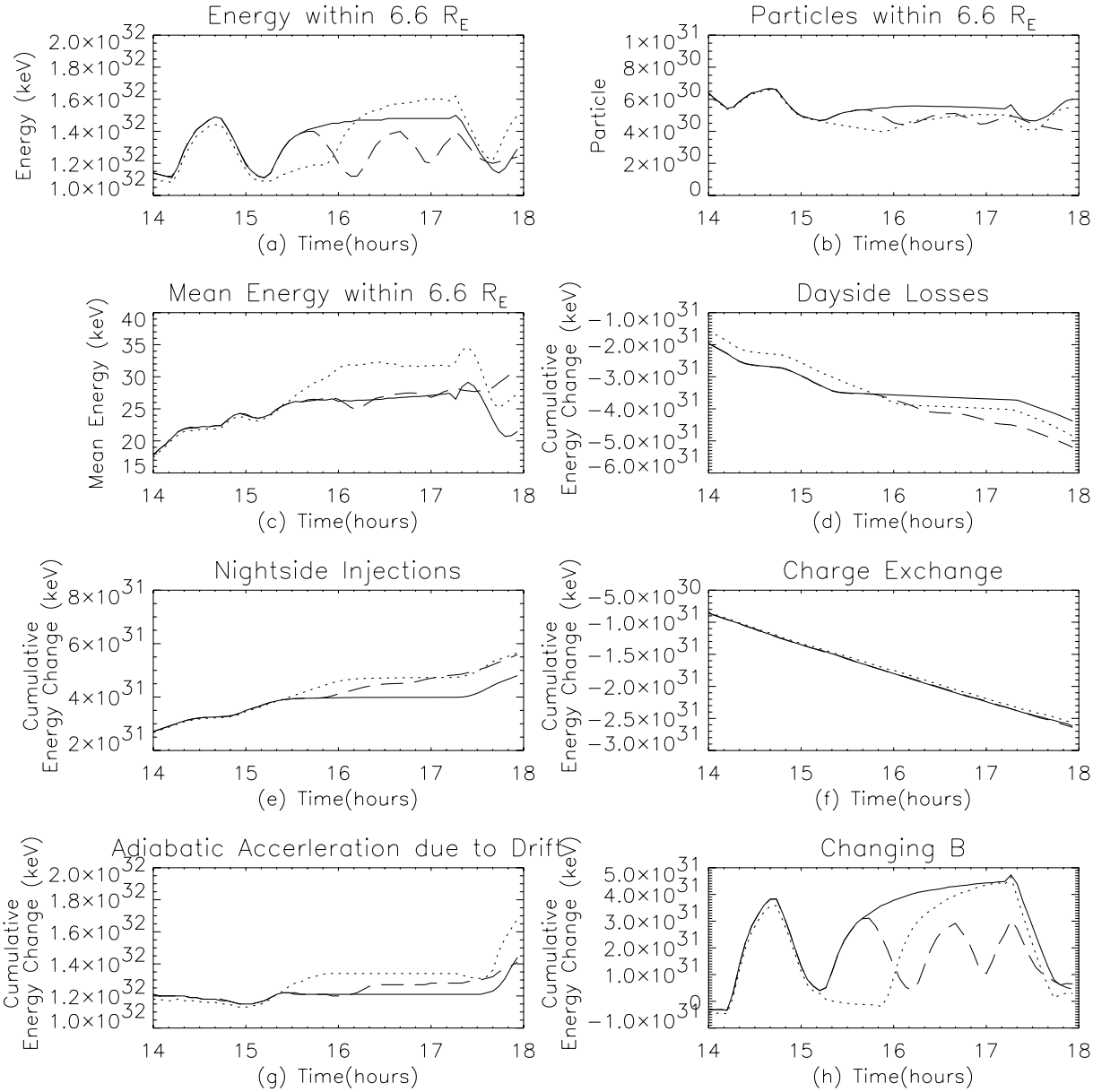

Figure 13. Case 1: solid line; case 2: dotted line; case 3: dashed line. (a) Total proton energy within 6.6 R_E; (b) number of particles within 6.6 R_E; (c) mean proton energy within 6.6 R_E; (d) accumulated energy changes on the dayside boundary; (e) accumulated energy changes on the nightside boundary (10 R_E); (f) accumulated energy changes due to charge exchange within 6.6 R_E; (g) accumulated energy changes due to adiabatic acceleration due to drift within 6.6 R_E; (h) accumulated energy changes due to the changing magnetic field within 6.6 R_E. Each plot has a different scale.

within geosynchronous orbit. This caused the total energy gain in case 3 to be less than case 2 even though the mean energy gain was larger. There are several contributions to the lower energy gain in case 3. Case 3 has a smaller cross polar cap potential after the second and third southward turnings than the average cross polar cap potential during southward IMF during case 2. Case 3 had fewer particles inside geosynchronous orbit. The model may underestimate the energy contribution due to depolarization, since the magnetic field changes in the MHD model inside 10 R_E during reconnection are relatively small.

[21] All cases show that energy is gained due to dipolarization in the tail and increases in ionospheric potential. The larger energy gain for the second injection in case 2 indicates that long periods of high ionospheric potential may contribute to larger energy gains for later substorms. The limited time between substorms in case 3 may contribute to lower energy gains for later substorms. Further study is required to determine if there is an optimal time between substorms for promoting energy gains in the ring current.

[22] **Acknowledgments.** We wish to thank Yusuke Ebihara for helpful discussions. We wish to thank Judy Johnson for her help with the 3-D visualization. Part of this work was performed while one of the authors (K.A.K) held a National Research Council Research Associateship Award

at Goddard Space Flight Center. Computations were performed at the Community Coordinated Modeling Center through the runs-on-request system.

[23] Lou-Chuang Lee thanks Masaki Ejiri for the assistance in evaluating this paper.

References

Akasofu, S.-I. (1968), *Polar and Magnetospheric Substorms*, Springer, New York.

Baker, D. N., and R. L. McPherron (1990), Extreme energetic decreases near geostationary orbit: A manifestation of current diversion within the inner plasma sheet, *J. Geophys. Res.*, *95*, 6591–6599.

Chen, M. W., L. R. Lyons, and M. Schulz (1994), Simulations of phase space distributions of storm time proton ring current, *J. Geophys. Res.*, *99*, 5745–5759.

Delcourt, D. C., and J. A. Sauvaud (1994), Plasma sheet ion energization during dipolarization events, *J. Geophys. Res.*, *99*, 97–108.

Ebihara, Y., and M. Ejiri (2000), Simulation study on fundamental properties of the storm-time ring current, *J. Geophys. Res.*, *105*, 15,843–15,860.

Fok, M.-C., and T. E. Moore (1997), Ring current modeling in a realistic magnetic field configuration, *Geophys. Res. Lett.*, *24*, 1775–1778.

Fok, M.-C., T. E. Moore, J. U. Kozyra, G. C. Ho, and D. C. Hamilton (1995), Three-dimensional ring current decay model, *J. Geophys. Res.*, *100*, 9619–9632.

Fok, M.-C., T. E. Moore, and M. E. Greenspan (1996), Ring current development during storm main phase, *J. Geophys. Res.*, *101*, 15,311–15,322.

Fok, M.-C., T. E. Moore, and D. C. Delcourt (1999), Modeling of inner plasma sheet and ring current during substorms, *J. Geophys. Res.*, *104*, 14,557–14,569.

Harel, M., R. A. Wolf, P. H. Reiff, R. W. Spiro, W. J. Burke, F. J. Rich, and M. Smiddy (1981), Quantitative simulation of a magnetospheric substorm, 1, Model logic and overview, *J. Geophys. Res.*, *86*, 2217–2241.

Jordanova, V., C. Farrugia, L. Janoo, J. Quinn, R. Torbert, K. Ogilvie, R. Lepping, J. Steinberg, D. McComas, and R. Belian (1998), October 1995 magnetic cloud and accompanying storm activity: Ring current evolution, *J. Geophys. Res.*, *103*, 79–92.

Kamide, Y. (1992), Is substorm occurrence a necessary condition for a magnetic storm?, *J. Geomagn. Geoelectr.*, *44*, 109–117.

Kozyra, J., V. Jordanova, J. Borovsky, M. Thomsen, D. Knipp, D. Evans, D. McComas, and T. Cayton (1998), Effects of a high-density plasma sheet on ring current development during the November 2–6, 1993, magnetic storm, *J. Geophys. Res.*, *103*, 26,285–26,306.

Liemohn, M. W., J. U. Kozyra, V. K. Jordanova, G. V. Khazanov, M. F. Thomsen, and T. E. Cayton (1999), Analysis of early phase ring current recovery mechanisms during geomagnetic storms, *Geophys. Res. Lett.*, *26*, 2845–2849.

Lui, A. T. Y., R. W. McEntire, and K. B. Baker (2001), A new insight on the cause of magnetic storms, *Geophys. Res. Lett.*, *28*, 3413–3416.

Powell, K. G., P. L. Roe, T. J. Linde, T. I. Gombosi, and D. L. De Zeeuw (1999), A solution-adaptive upwind scheme for ideal magnetohydrodynamics, *J. Comput. Phys.*, *154*(2), 284–309.

Reeves, G. D., and M. G. Henderson (2001), The storm-substorm relationship: Ion injections in geosynchronous measurements and composite energetic neutral atom images, *J. Geophys. Res.*, *106*, 5833–5844.

Reeves, G. D., et al. (2004), IMAGE, POLAR, and geosynchronous observations of substorm and ring current ion injections, in *Disturbances in Geospace: The Storm-Substorm Relationship*, *Geophys. Monogr. Ser.*, vol. 142, edited by A. S. Sharma, Y. Kamide, and G. S. Lakhina, pp. 91–101, AGU, Washington, D. C.

Sauvaud, J. A., T. Beutier, and D. Delcourt (1996), On the origin of flux dropouts near geosynchronous orbit during the growth phase of substorms: 1. Betatron effects, *J. Geophys. Res.*, *101*, 19,911–19,919.

Sheldon, R. B., and D. C. Hamilton (1993), Ion transport and loss in the Earth's quiet ring current: 1. Data and standard model, *J. Geophys. Res.*, *98*, 13,491–13,508.

Wolf, R. A., and M. Harel (1979), Dynamics of the Magnetospheric Plasma, in *Dynamics of the Magnetosphere*, edited by S.-I. Akosofu, pp. 143–163, Springer, New York.

Wolf, R. A., J. W. Freeman Jr., B. A. Hausman, R. W. Spiro, R. V. Hilmer, and R. L. Lambour (1997), Modeling convection effects in magnetic storms, in *Magnetic Storms*, *Geophys. Monogr. Ser.*, vol. 98, edited by B. T. Tsurutani et al., pp. 161–172, AGU, Washington, D. C.

D. L. DeZeeuw and T. I. Gombosi, Space Physics Research Laboratory, University of Michigan, 2455 Hayward, Ann Arbor, MI 48109-2143, USA.

M.-C. Fok, NASA Goddard Space Flight Center, Code 612.2, Greenbelt, MD 20771, USA. (mei-ching.h.fok@nasa.gov)

M. Hesse, M. M. Kuznetsova, A. Narock, and L. Rastaetter, NASA Goddard Space Flight Center, Code 612.3, Greenbelt, MD 20771, USA.

K. A. Keller, 13815H Braddock Springs Road, Centreville, VA 20121, USA.